Origins and Implications of Intrinsic Stress in Hydrogenated Amorphous Silicon Thin Films

by

Eric Johlin

Submitted to the
Department of Mechanical Engineering
in Partial Fulfillment of the Requirements for the Degree of

Master of Science in Mechanical Engineering

at the

Massachusetts Institute of Technology

September 2012

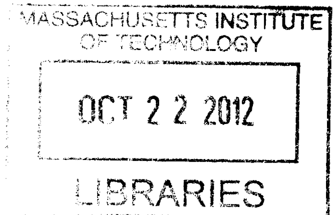

© 2012 Massachusetts Institute of Technology. All rights reserved.

Signature of Author: ______________________
Department of Mechanical Engineering
August 24, 2012

Certified by: ______________________
Prof. Jeffrey C. Grossman
Associate Professor of Materials Science and Engineering
Thesis Supervisor

Certified by: ______________________
Prof. Tonio Buonassisi
Associate Professor of Mechanical Engineering
Thesis Supervisor

Accepted by: ______________________
David Hardt, Professor of Mechanical Engineering
Chairman, Department Committee on Graduate Theses

Origins and Implications of Intrinsic Stress in Hydrogenated Amorphous Silicon Thin Films

by

Eric Johlin

Submitted to the Department of Mechanical Engineering
on August 24, 2012, in Partial Fulfillment of the
Requirements for the Degree of
Master of Science in Mechanical Engineering

ABSTRACT

Despite decades of research on hydrogenated amorphous silicon (a-Si:H), there remains much to be understood about the relationship between deposition conditions and the resulting structural, optical, and bulk properties of the material. In this work we investigate these correlations for a-Si:H films created using plasma enhanced chemical vapor deposition (PECVD), focusing on the creation of intrinsic stresses within the films. Through experimental examination of the deposition process pressure, we model the plasma ion momentum using a combination of theoretical models and empirical trends. We find that compressive stress is controlled by ion bombardment causing of peening the film, and leading to lattice distortion in the material. Conversely, tensile stress is created through bombarding ions collapsing nano-sized voids within the material, which are formed during the vapor-phase deposition. Combining our model of ion momentum with the theory of ion peening creating compressive stress, we are able to fit the process conditions to the observed the compressive regime of our films. Furthermore, by analyzing the hydrogen content in voids within our films, we are able to predict the film porosity, and thereby model the void collapse, yielding the tensile stresses. The balance between these compressive and tensile stress forces determines the final intrinsic stress state, and allows our refined model to fit the entire range of highly compressive to highly tensile film stresses. Finally, we present correlations between film structural properties and observed optical properties, real and imaginary refractive indices and optical band gap, factors important for the creation of a-Si:H based devices.

Thesis Supervisors:
Jeffrey C. Grossman
Title: Associate Professor of Materials Science and Engineering

Tonio Buonassisi
Title: Associate Professor of Mechanical Engineering

DEDICATION

This work is dedicated to my parents, and all my friends who were so incredibly supportive throughout my academic career.

TABLE OF CONTENTS

Abstract 3

Dedication 5

Table of Contents 7

Figures and Tables 9

1. Introduction 11

 1.1. Motivation for the Study of Hydrogenated Amorphous Silicon 11

 1.2. Motivation for the Study of Stress 13

2. Materials and Methods 15

 2.1. Film Deposition 15

 2.2. Film Stress Measurements 17

 2.3. Thickness and Optical Bandgap Measurements 19

 2.4. Optical Constants and Film Density Measurements 20

 2.5. Hydrogen Content and Bonding Configuration Measurement 21

3. Results and Discussion 25

 3.1. Origins of Stress 26

 3.2. Modeling Ion Bombardment through PECVD Conditions 33

3.3. Implantation Effects on Stress 35

3.4. Void Collapse Effects on Stress 38

3.5. Correlation between Film Density and Optical Properties 43

3.6. Failure of Stressed a-Si Films 47

4. Conclusions and Future Work 49

4.1. Conclusions 49

4.2. Future Work 50

Appendix 53

Acknowledgements 55

References 57

FIGURES AND TABLES

Figure 2.1.1 Deposition rate as a function of process pressure 16

Figure 2.5.1 Cartoon illustration of hydrogen bonding configurations 22

Figure 2.5.2 Measurement of hydrogen content from FTIR absorption........................... 23

Figure 2.5.3 FTIR absorption of films under differing stress states 24

Figure 3.1.1. Correlation between process pressure and measured film stress................. 28

Figure 3.1.2. Optical micrographs of films exhibiting failure 29

Figure 3.1.3 Depiction of structural modifications leading to stress creation 31

Figure 3.3.1. Film density with respect to deposition ion momentum 37

Figure 3.4.1. Film intrinsic stress as a function of ion momentum 39

Figure 3.5.1 Optical properties as a function of stress and density 44

Figure 3.5.2 Relationship between hydrogen void concentration and film density.......... 46

Table 0.1 Film properties of representative samples 53

CHAPTER

1

INTRODUCTION

1.1. Motivation for the Study of Hydrogenated Amorphous Silicon

As the global energy infrastructure shifts due to the rising demand for clean, renewable energy, solar power is playing an increasingly substantial role in energy production. A variety of systems to create this power are currently in use and further development, each with its own inherent advantages and disadvantages. The current frontrunner, from an installation and production standpoint, are photovoltaic devices made with crystalline silicon bulk absorber layers, controlling more than 60% of the US market, and more than 80% of the global installed capacity.[1,2]

Although silicon is one of the most abundant elements on earth, the cost of the crystalline silicon material in the these photovoltaic devices contributes considerably to the final price of the solar cell.[1] Unlike the currently more popular crystalline silicon,

hydrogenated amorphous silicon (a-Si:H) is not an indirect band gap semiconductor, allowing photovoltaic (PV) devices made from a-Si:H to absorb light much more readily, and thus can be made with orders of magnitude less material. This, combined with the already lower price of amorphous silicon, significantly decreases the largest barrier to widespread PV adoption: the high relative cost of these devices. Furthermore, the thinness of a-Si:H devices provides potential for non-standard configurations (curved and flexible devices), allowing novel applications of PV. While this makes a-Si:H an extremely attractive material for solar cell production, the major barrier to its widespread adoption is the low device efficiency.

While hydrogenated amorphous silicon has a multitude of other applications as well, many of which are currently in wide use (thin film transistors, crystalline silicon passivation layers, optical waveguides, *etc.*), the possibly most momentous aspect of the material is its scholastic significance – as the most studied amorphous solid,[3] any elucidation of the material can be seen as representative of the improvement in knowledge of the entire class of matter. Furthermore, the vast frontier of knowledge still remaining to be discovered for amorphous silicon makes the study that much more exciting.

1.2. Motivation for the Study of Stress

Prior attempts to investigate the influence of stress in a-Si:H films were mostly conducted by mechanically loading thin-film devices at room temperature.[4–7] Electron mobility (μ) was observed to follow the relation $\mu = \mu_0(1 + 26\times\varepsilon)$, where ε is strain (positive = tensile).[4] Such films plastically deformed at strains as low as ±0.2% (stresses of ±400 MPa), resulting in declining cell performance.[5] Other researchers observed changes in intrinsic stress as a function of growth conditions, particularly process pressure.[8–11] At deposition temperatures around 200°C, atomic configuration can be more easily altered without catastrophic film failure. For instance, Wehrspohn *et al.*[8] varied the SiH_4 partial pressure during plasma-enhanced chemical vapor deposition (PECVD) with a 2:1 H_2 dilution, resulting in intrinsic stresses in the range of -650 to +300 MPa in films grown at 210°C.

While these works have advanced the initial understanding of how stress modifies the properties of the material, the core process-structure-property relationships of the material remain unclear. This study works to alleviate the uncertainty in these relationships in three ways: First, we explore the underlying physical origin of the intrinsic stresses present in amorphous silicon films deposited by plasma enhanced chemical vapor deposition (PECVD). By combining a mixture of theoretical models gleaned from the existing literature on the material with empirical models derived from our own experiments, along with physical intuition of the atomic processing of the

deposition, we are able to coalesce a comprehensive explanation for the expression of the multitude of stress states present in the material, and model the differing stress levels throughout the entire observed range. Second, through the extension of this model we are able to not only relate the deposition conditions directly to the measured structural properties, but also explain their creation. Third, and finally, we relate the observed structural states of the materials to the observed bulk properties, such as the refractive indices and optical bandgap. Based on our findings, we speculate on means to decouple deposition rate from film stress, towards high-throughput production of higher-quality a-Si films.

CHAPTER

2

MATERIALS AND METHODS

2.1. Film Deposition

In this study, all amorphous silicon thin films were deposited on circular three-inch (76 mm) diameter p-type (100) crystalline silicon substrates. The circular geometry is advantageous for two reasons: First, when calculating stress via curvature measurements, the circular geometry prevents the formation of non-uniform stress fields due to the free surfaces meeting at corners present in non-circular substrates. Second, the circular substrate limits the special dependence of the thickness of the deposition (due to both the physical edges of the substrate interacting with the plasma, as well as the full substrate causing non-linearity in the field across the substrate during deposition) to one dimension (radial) whereas non-circular substrates would induce a two-dimensional spatial dependence in the deposition thickness across the substrate. The choice of crystalline silicon as the substrate was used to both minimizes thermal stresses due to

similar coefficients of thermal expansion, as well as allow close lattice matching between the substrate and neutral-stressed film material.

Prior to thin-film deposition, wafers were cleaned using an SC1 etch (1:1:5 H_2O_2:NH_4OH:H_2O), followed by an oxide strip (hydrofluoric acid in a 7:1 buffer solution), and finally an SC2 etch (1:5:1 H_2O_2:H_2O:H_2SO_4). Between each step of the cleaning process, the substrates were rinsed in three cycles of deionized water to ensure complete removal of chemicals used prior.

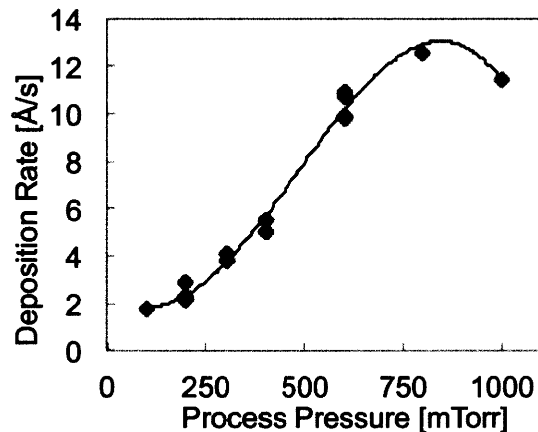

Figure 2.1.1 Deposition rate as a function of process pressure

Calculated PECVD deposition rate of a-Si:H with respect to the chamber pressure during deposition. The solid line is intended as a guide to the eye.

Amorphous silicon films were deposited using a PECVD tool built by Surface Technology Systems. This tool operates with an RF frequency of 13.56 MHz, and deposits on a 182.4 cm^2 platen. Prior to deposition, a film of 200 nm of silicon-oxide was deposited in order to both electrically isolate the film from the substrate as well as

prelude the diffusion of dopants from the crystalline silicon wafer into the amorphous silicon film. The a-Si depositions were performed with a 200°C substrate temperature, 55 sccm SiH_4 flow rate, and with no argon flow, and a 200 mTorr default process pressure, with 30 W of discharge power to the plasma. These parameters were chosen (and verified) to prevent any possible formation of micro- or nano-crystalline silicon within the films. From this standard recipe, several samples were deposited testing the extremes of each process condition, ensuring that for each, the film (at least partially) adhered to the substrate surface. The effect of different discharge powers was examined (20–35 W), but the limited available range was not sufficient to influence our conclusions. Deposition rates were determined for each process condition by depositing several films at varying times, and measuring the resulting film thicknesses using ellipsometry (see Chapter 2.3). Calculated deposition rates (1.8–12.6 Å/s, presented in Figure 2.1.1) are within range of commercial solar cell manufacturing. The widest range of available stress states was observed through the modification of the process pressure, and so this variable was chosen to be isolated for the experiments present in this work.

2.2. Film Stress Measurements

A stressed thin film will induce strain in the substrate to which it is adhered, resulting in a curvature of the ensemble. Because the film is thin compared to the substrate, stress is approximated as uniform throughout the film thickness. Film stress can

be inferred by measuring the substrate curvature prior to and after thin-film deposition. Using Stoney's formula,[12] the change in curvature ($\Delta\kappa$) can be related to the induced film stress (σ_{m}) as

$$\sigma_{\mathrm{m}} = \frac{M_{\mathrm{s}} h_{\mathrm{s}}^2}{6 h_{\mathrm{f}}} \Delta\kappa \, , \qquad [1]$$

where M_{s} is the substrate biaxial elastic modulus, and h_{s} and h_{f} are the substrate and film thicknesses, respectively. This formula assumes that: (1) the distributed line force and the induced deformation are axially symmetric; (2) the distributed line force induces a plane stress state; (3) edge effects are negligible; (4) strain is isotropic and curvature is uniform, resulting in a spherical deformation of the a-Si/substrate bilayer.

Curvature measurements were performed using a Toho FLX-2320-S. The tool determines curvature by rastering a laser along an axis on the sample surface while an optical detector measures changes in angle of the reflected laser beam. Only the inner 60 mm across the diameter of each bilayer was considered, to avoid edge effects. Each sample was measured in at least two orientations, to confirm the validity of assumptions used in Stoney's formulation. The change of curvature is given as

$$\Delta\kappa = \frac{1}{R_{\mathrm{f}}} - \frac{1}{R_{\mathrm{i}}} \, , \qquad [2]$$

where R_{f} and R_{i} represent the post- and pre-deposition radii of curvature of the substrate, respectively. Measurements of curvature were taken on the bare substrate, after silicon-oxide film deposition, and again after a-Si:H film deposition. Amorphous silicon film

stress is inferred by measuring the change in substrate curvature before and after a-Si deposition.

2.3. Thickness and Optical Bandgap Measurements

Measurements of film refractive indices were obtained using a variable-angle spectroscopic elliposometer (M-2000XI, J.A. Woollam). Ellipsometry directly measures the ratio, ρ_r, of the plane wave electric field components perpendicular and parallel to the incident plane. This can be parameterized into an equation of the amplitude upon reflection, *tan[ψ]*, and the phase shift through the material, Δ, through the equation $\rho_r = \tan(\psi)e^{i\Delta}$.[13] From these measurements, film thickness and optical constants were calculated using the *Tauc-Lorentz* model to fit the obtained spectra a system model comprised of a c-Si "infinite" substrate, silicon oxide layer, a-Si thin film, and native silicon oxide structure.

From optical constants measured by ellispometry, the real and imaginary terms of the refractive index (n, k) and the wavelength of light in air (λ) can be used to calculate the absorption coefficient (α) for the thin films, using the equation $\alpha = 4\pi k / \lambda$. In accord with the method presented by Hishikawa,[14] the optical gap for all films was determined by fitting the linear region (~60% of our curves) of the relationship

$(n\alpha h\nu)^{1/3} = B\left(h\nu - E_g\right)$, where E_g is the optical bandgap, and h, B are Planck's constant and the constant related to the slope of the absorption plot, respectively.

2.4. Optical Constants and Film Density Measurements

Nondestructive film density measurements can be performed via optical means. The Clausius-Mossotti relation describes the interaction between the index of refraction n, and film density, ρ

$$\frac{n^2-1}{n^2+2} = \frac{4\pi\rho}{3M} Na \ , \qquad [3]$$

where M is the atomic mass of Si, N is Avogadro's number, and a is the atomic polarizability of the film. In order to evaluate the expression, one must first be able to compute the atomic polarizability, requiring knowledge of the total hydrogen content (c_{H}) of the film. This can be obtained through the expanded equation put forward by Remes,[15]

$$\frac{n^2-1}{n^2+2} = \frac{4\pi\rho}{3M} N\left(2a_{\text{Si-Si}} + \frac{c_{\mathrm{H}}}{1-c_{\mathrm{H}}}\left(a_{\text{Si-H}} - \frac{a_{\text{Si-Si}}}{2}\right)\right), \qquad [4]$$

using the values of $a_{\text{Si-Si}} = 1.96\times10^{-24}\,\mathrm{cm}^3$ and $a_{\text{Si-H}} = 1.36\times10^{-24}\,\mathrm{cm}^3$ for the polarizability of the Si–Si and Si–H bonds, respectively. To evaluate this equation though,

one clearly must know the total film hydrogen content.

2.5. Hydrogen Content and Bonding Configuration Measurement

To determine the hydrogen content of our films, absorption spectra using Fourier transformed infrared (FTIR) spectroscopy (PerkinElmer Spectrum 400 FT-IR spectrometer) was employed. By investigating hydrogen streaching modes, corresponding to peaks at 2000 and 2090 cm^{-1}, the amount of hydrogen bonded in a silicon-monohydride configuration, and in polyhydride or clustered voids, respectively, can be obtained. These bonding configurations are illustrated in Figure 2.5.1.

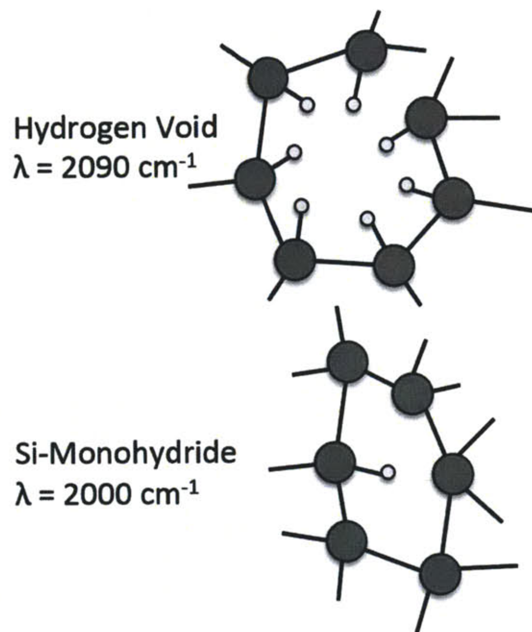

Figure 2.5.1 Cartoon illustration of hydrogen bonding configurations

Atomic configurations of hydrogenated nanovoids (top), corresponding to the 2090 cm^{-1} peak, and silicon monohyride (bottom), corresponding to the 2000 cm^{-1} peak, where the grey circles represent silicon atoms, and the white represent hydrogen.

Due to the proximity of these absorption modes, it is necessary to fit two Gaussian peaks to the obtained spectrum data in order to deconvolve the two modes, as depicted in Figure 2.5.2 and Figure 2.5.3. By integrating the area under the fit to the 2000 cm^{-1} peak, and normalizing the value to the fit parameter $9.0*10^{19}$ cm^{-2}, the amount of hydrogen per cubic centimeter in the Si-H configuration is obtained, while integrating under the 2090 cm^{-1} peak, and using the fit parameter $2.2*10^{20}$ cm^{-2} yields the density of hydrogen either passivating the walls of nanovoids, or in polyhydride configurations.[16] Finally, as the measurement of the concentration at the 2100 cm^{-1} peak is proportional to

the presence of nanovoids in the material, this measurement gives a prediction of the porosity of the film.

After the concentrations of these two hydrogen modes have been calculated, Eqs. 3 and 4 can be iterated in order to calculate the density and absorption coefficient of the materials.[16–20]

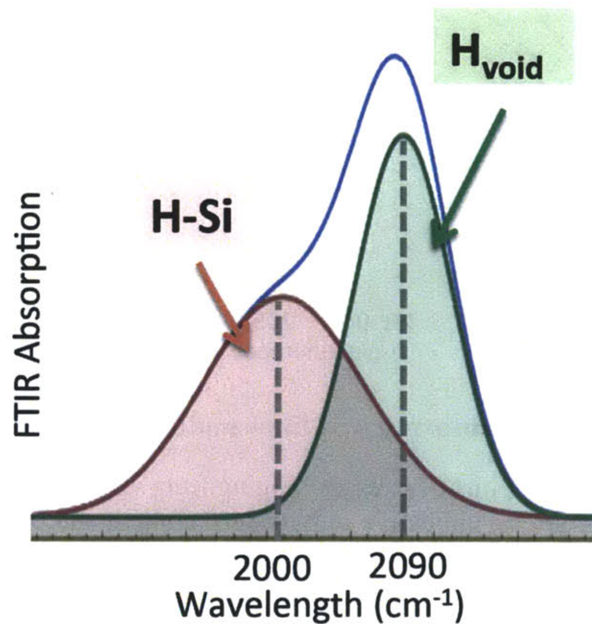

Figure 2.5.2 Measurement of hydrogen content from FTIR absorption

Depiction of the calculation of hydrogen content in the two bonding configurations (silicon monohydride and hydrogenated voids) by fitting Gaussian peaks to FTIR absorption spectra.

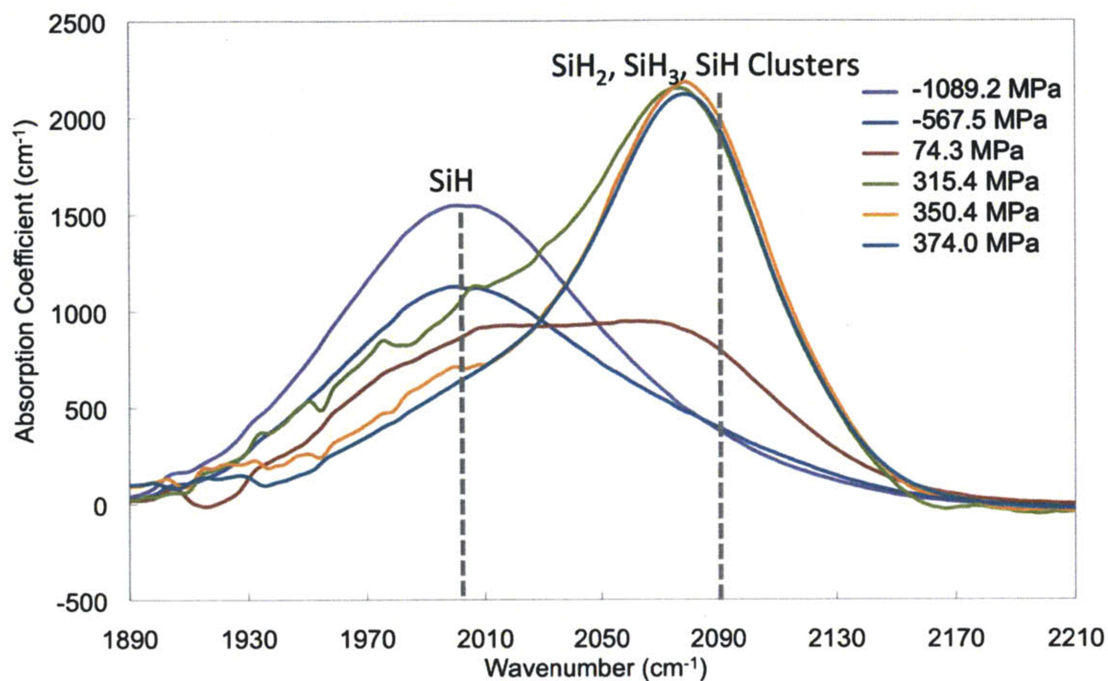

Figure 2.5.3 FTIR absorption of films under differing stress states

FTIR Absorption peaks of films of stresses ranging from -1089 MPa compressive stress to +374 MPa of tensile stress, indicative of hydrogen content and bonding configurations

CHAPTER 3

RESULTS AND DISCUSSION

Using the methods outlined in the previous chapters, we now work to combine the acquired relationships between our samples in a meaningful way. This will be presented in six sections:

In sections one and two, the basis for our stress model will be presented, including the overall observed trends, exclusion of possible parameters found to be implausible for the stress creation, and the control of stress to a single relevant process parameter, ion momentum.

In the third section we begin our investigation of the components relevant to the stress creation through the ion momentum parameter by modeling the ion bombardment effect on stress in our films. This allows us to capture the *compressive* stress effects observed.

* Please note that this chapter contains copyrighted information, reproduced with permission from the American Physical Society.

Reference: E. Johlin, N. Tabet, S. Castro-Galnares, A. Abdallah, M.I. Bertoni, T. Asafa, J.C. Grossman, S. Said, and T. Buonassisi, Physical Review B **85**, 075202 (2012).²¹

Reference: E. Johlin, N. Tabet, S. Castro-Galnares, A. Abdallah, M.I. Bertoni, T. Asafa, J.C. Grossman, S. Said, and T. Buonassisi, Physical Review B 85, 075202 (2012).²¹

Section four works to include the observed tensile stress states in our films through modeling the ion bombardment-induced void collapse. This section introduces the net stress state as a balance between the presented compressive and tensile effects, and generalizes our model to fit over the entire observed range of stresses.

In the final two sections (five and six) we correlate the controlled process parameters (here, process pressure) to the film microstructure (density, and void content) and then these aspects to the observed bulk film properties present (refractive indices, and optical bandgap). We believe these correlations should be useful in engineering desired properties into amorphous silicon films for many applications (passivation, waveguides, *etc.*).

3.1. Origins of Stress

The observed total stresses in our films range from -1230 (compressive) to +393 MPa (tensile). We first examine these stress states by calculating the contribution of thermal stresses to the total stress. As presented by Wehrspohn[8], we compute the influence of thermal stress, σ_T, by the equation

$$\sigma_T = \frac{Y_F}{1-\nu_F}(\alpha_F - \alpha_S)(T_{dep} - T_{meas}), \qquad [5]$$

where Y_F is the Young's modulus of the film, v_F is the films Poisson ratio, α_F and α_S are the thermal expansion coefficients of the film and substrate, respectively, and T_{dep} and T_{meas} are the deposition and measurement temperatures. Values for the Young's modulus of amorphous silicon are reported to rang from between 110 to 150 GPa. An intermediate value of 130 GPa was used for our calculations.[8] The Poisson ratio is reported to be ~0.2, and invariant with film composition.[8] Thermal expansion coefficients of amorphous silicon and crystalline silicon are reported as 3.7 and 3.28 (10^{-6} K^{-1}), respectively.[8] Our deposition temperature of 200°C, and measurement temperature of 23°C give us thermal stresses in the range of +6.8 and +14.3 MPa. These are clearly minuscule when compared to the ~1-2 orders of magnitude larger total stresses, and so we conclude our films are being dominated by the intrinsic stress, computed through the equation

$$\sigma_{Int} = \sigma_{Total} - \sigma_T . \qquad [6]$$

The intrinsic stresses in our films (calculated through Eqs. 5 and 6) range from -1253 to +387 MPa (shown in Figure 3.1.1). Stresses above +387 MPa (more tensile) resulted in film delamination, as shown in Figure 3.1.2b, while stressed below -1253MPa (more compressive) resulted in film buckling, as shown in Figure 3.1.2a.

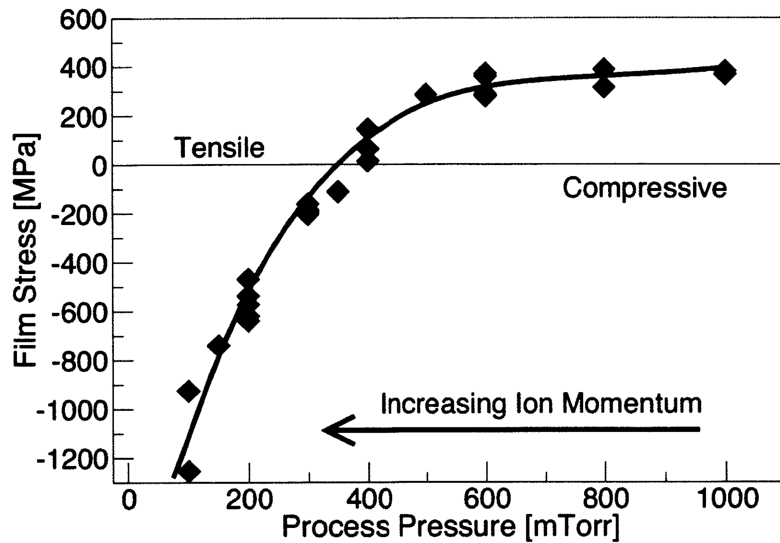

Figure 3.1.1. Correlation between process pressure and measured film stress

The solid line displays the correlation with the net stress model, as described in Sec. III-D, and the thin line through the origin simply denotes the transition between net tensile and compressive stress. Figure reprinted from Ref. 21.

Intrinsic stresses in amorphous thin films arise from systematic modifications of atomic positions after a slip-free adhesion layer forms with the substrate.[22] Such changes in atomic arrangement can be tailored by specific growth conditions. The PECVD input variables observed to exert the greatest influence on thin-film stress are deposition temperature,[8] hydrogen dilution,[23] plasma frequency,[10] discharge power,[24–26] and ambient gas pressure.[8]

The influence of these deposition parameters on film structure consequently alters the mechanical and optoelectronic properties of the cells. In this study we isolate the influence of gas pressure.

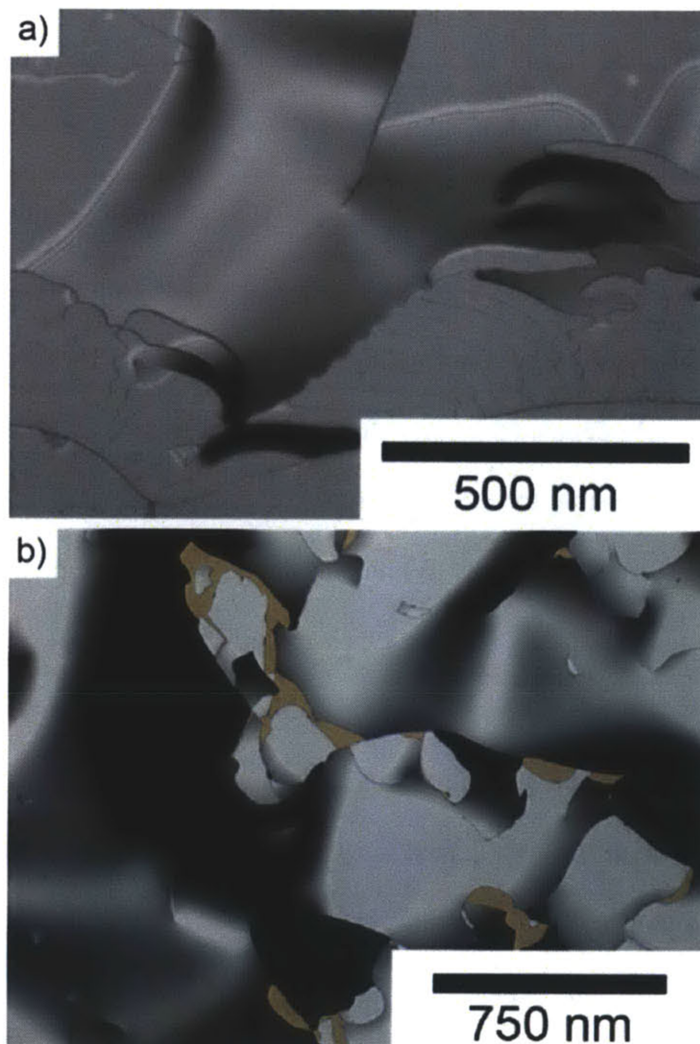

Figure 3.1.2. Optical micrographs of films exhibiting failure

(a) compressive stress buckling, estimated around -1200 MPa, and (b) tensile stress delamination, estimated around +450 MPa. Figure reprinted from Ref. 21.

The origin of stress in our films is likely due to an *ion bombardment effect*,[8,24,27] which has been previously reported in films deposited by both ion sputtering and[27,28]

PECVD,[8,25] relating internal stresses of films to the momentum of the depositing ions. Based on models put forth by Windischmann[28] and Smets,[29] we are able to describe the observed stress behavior purely through ion interactions with the depositing film and correlate these descriptive models to the observed experimental data.

Intrinsic stress in amorphous silicon thin films can be viewed as a balance between two distinct but competing forces: the collapse of hydrogenated nanovoids after being formed on the depositing layer creating tensile stresses,[30,31] and the implantation of ions into the previously deposited layers[32] (often referred to as "ion peening") leading to lattice expansion, responsible for the creation of compressive stresses in the film (both of which are illustrated in Figure 3.1.3). While plasma ion momentum dictates both of these forces, it is their relative strength at any given momentum level that determines the net intrinsic stress state of the film. Specifically, at low average ion momentum levels (for example, at high deposition pressure), the contribution of nanovoid collapse (either through interaction with the non-depositing ion plasma while still near the surface, or through ion injection collapsing more deeply buried voids) easily outweighs the compressive effects of bulk expansion from the relatively rare deep ion implantations, and thereby produces a film of net tensile stress. Conversely, with high ion momentum (low pressure), a substantially larger number of ions are implanted into the bulk of the film, resulting in a strong compressive stress component, outweighing the tensile stress from the collapse of nanovoids (especially as the voids available for collapse are inherently finite, whereas the limit to compressive stress from implantation does not contain such an abrupt limitation), and creating a net compressively stressed film. From

these descriptions we conclude that our process conditions are determining the ion momentum of deposition, controlling both the collapse of nanovoids, and ion peening in our films, the balance of which is in turn dictating our film structure and intrinsic stress.

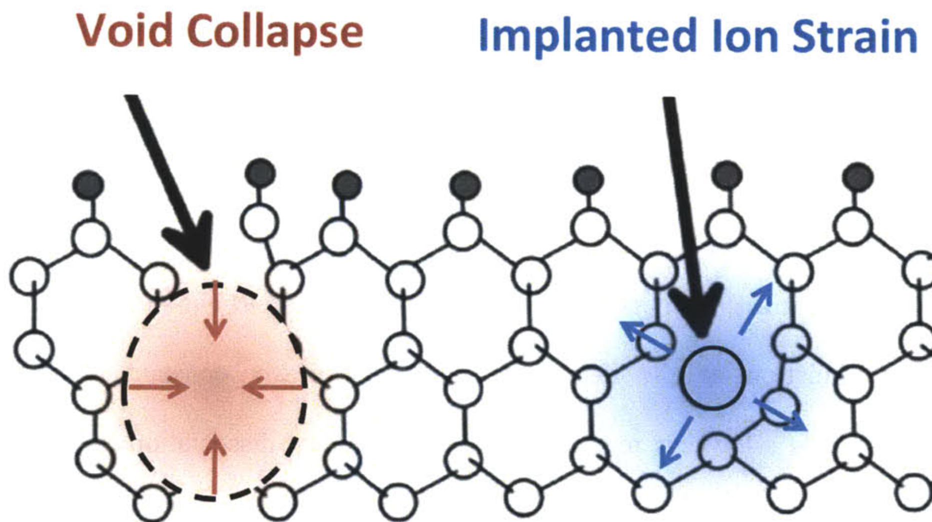

Figure 3.1.3 Depiction of structural modifications leading to stress creation

Illustration of void collapse (left), leading to the formation of tensile stress, and implanted ion strain (right) causing the creation of compressive stress. Adapted from Ref. [29]

We justify the exclusive examination of ion bombardment-induced stresses through the elimination of all other plausible causes of stress in the material: given the growth parameters used in the present study, we exclude *surface stresses*[33] and *coalescence stresses,*[12,23] which dominate at film thicknesses of single nanometers. *Hydrogen and hydrogen-induced bond reconstruction*[34] models are precluded due to the

observation of a strong tensile stress regime, as well as the lack of causal analysis present in these theories (see Chapter 3.3). Nanocomposite effects[23] can also be reasonably concluded to play a negligible role as the growth temperature and hydrogen dilution ratios are too low to induce a partial phase transition to microcrystalline silicon.[35] Furthermore, we observe no evidence of embedded nanocrystals in the amorphous Si matrix via grazing-incidence X-ray diffraction. Finally, film compositional variations could be observed though changes in the deposition gas due to *silane dissociation*. However, results from Gallagher[36] indicate that for similar process conditions, deposition is dominated (>98%) by SiH_3 radicals, indicating that modifications to pressure and power could thus influence deposition rate (which is observed) but should not affect the chemical formulation of the depositing gas. This nearly constant deposition gas stoichiometry thus allows us to reasonably conclude that dissociation does not play a major role in the modification of structural properties in our study, although should likely be examined in those significantly varying deposition power or discharge frequency.

The remainder of this section is devoted to the elucidation of the ion bombardment model through the exploration of microstructural film properties, and the amalgamation of empirical and theoretical correlations. We will proceed in three steps: first, we will establish a numerical calculation of ion momentum (the property responsible for the control of ion bombardment) from our deposition conditions. Next, we will present a modified theoretical model of the compressive stress forces from the literature. Finally, we empirically include the tensile stress influences into our model by fitting the experimentally measured reduction in hydrogen void concentration.

3.2. Modeling Ion Bombardment through PECVD Conditions

To begin the numerical exploration of qualitative model described in the previous subsection, we calculate the average incident ion momentum through its relation to the average ion energy in the equation

$$\bar{p}_{\text{ion}} = \sqrt{2M\bar{E}_{\text{ion}}}, \qquad [7]$$

where M is the ion mass and $\bar{p}_{\text{ion}}$ is the average ion momentum. Through a reformulation of the theory proposed by Lee *et al.*,[24] average ion energy flux, $\bar{E}_{\text{ion}}$, can determined to vary as

$$\bar{E}_{\text{ion}} = \frac{qI_{\text{rms}}\lambda\cos\beta}{\omega\varepsilon_0 A_p}, \qquad [8]$$

where q is the electron charge, I_{rms} is the room mean square of the plasma current, λ is the mean free path of ions in the plasma, $\cos\beta$ the collision angle between the electric field and direction of ion propagation in the plasma (assumed 0.5, per Lee[24]), ω frequency (equal to $2\pi f$, where f is the nominal plasma frequency), ε_0 vacuum

permittivity, and A_p is the electrode area. Here, ω and A_p are constant for all depositions. Translating I_{rms} into discharge power, W, and pressure in the deposition chamber, P, per the formulation presented by Catherine[37], we obtain

$$\bar{p}_{ion} = \sqrt{2M\frac{q\lambda\sqrt{WP}\cos\beta}{\omega\varepsilon_0 A_p}}. \qquad [9]$$

Combining these variables with q and ε_0 into a constant term C, we are left with an expression for ion momentum as a function of our controllable deposition parameters and the ion mass and ion mean free path,

$$\bar{p}_{ion} = C\sqrt{M\lambda\sqrt{\frac{WP}{\omega}}}. \qquad [10]$$

The ion mean free path (λ) is inversely proportional to both the gas density and pressure present at deposition. Combining this relation with Eq. 10, results in our final formula for the ion momentum,

$$\bar{p}_{ion} \propto \left(\frac{W}{\omega P}\right)^{1/4}, \qquad [11]$$

showing a (-1/4) power dependence of process pressure on ion momentum, and allowing the relative determination of $\bar{p}_{ion}$ through our deposition conditions.

3.3. Implantation Effects on Stress

The direct relationship between compressive (bulk-implantation process) stress and ion momentum in sputtered films has been modeled theoretically by Davis,[32] yielding a proportionality of

$$\sigma \propto \frac{Y}{(1-\nu)} \frac{\bar{p}_{\text{ion}}}{R/j + k\bar{E}_{\text{ion}}^{5/3}}, \qquad [12]$$

where σ is the film stress, Y the Young's modulus, ν the Poisson ratio, $\bar{E}_{\text{ion}}$ is the deposition ion energy, $\bar{p}_{\text{ion}}$ is the average ion momentum, R/j is the ratio of deposition film flux to ion bombarding flux, and k is a constant material parameter. Following the analysis from Yi,[24] our PECVD deposition conditions will yield large R/j values (the majority of collisions with the film will be normal depositing collisions not bombardment collisions, in contrast to sputtering where the bombardment component can easily dominate that of deposition), and furthermore, due to our lack of argon dilution, the number of bombardment collisions should be at least roughly proportional to the total collisions. This, in agreement with calculations by Yi, [24] causes the stress to scale simply as

$$\sigma \propto \frac{Y}{(1-\nu)} \bar{p}_{\text{ion}}. \qquad [13]$$

It is important to note that this stress-momentum model applies to only the bulk (compressive) stress effects due to particle bombardment in fully densified films, free from microstructure modification, and thus with constant mechanical properties (Y and ν). To generalize this model further, we examine the dependence of the mechanical properties of the films on the evolving density.

Film Young's modulus in amorphous silicon has been modeled by Miranda *et al.*[38] to vary with a 2.5 power dependence on film density. The Poisson's ratio has been shown by Wehrspohn *et al.*[8] to remain virtually invariant across films of varying hydrogen content, and, through our examination, across all possible values (0 – ~0.3) imparts little change on the values obtained by Eq. 13. Combining these theories with Eq. 13, we are left with the equation

$$\sigma \propto \rho^{2.5} \bar{p}_{\text{ion}}. \qquad [14]$$

We validate our model by utilizing our experimental trend between density and ion momentum (fit simply to a second-order polynomial function, which, although not fit perfectly, does allow for the general influence of ion momentum on density to be incorporated) shown in Fig. 7, to fit Eq. 14 to only one experimental variable ($\bar{p}_{\text{ion}}$). This final model of compressive stress is shown fit to our independently measured experimental stress data as the dashed line in Figure 3.4.1a, matching a similar trend observed by Hamers. [39]. One can note that the correlation between the model and experiment clearly breaks down in region I of the plot. This, however, can be accounted

for through the inclusion of void collapse (tensile stress) effects (see Chapter 3.4).

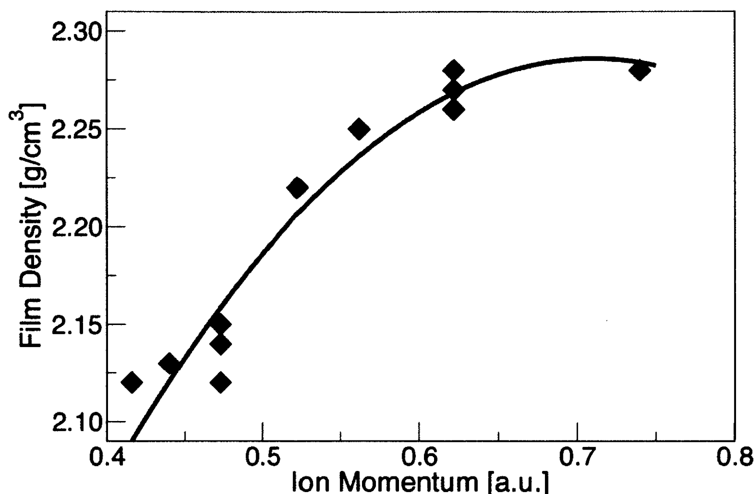

Figure 3.3.1. Film density with respect to deposition ion momentum

Film density (determined optically) with respect to deposition ion momentum, shown with the second-order polynomial fit used for the inclusion of the evolving mechanical properties of films in Eq. 14. Figure reprinted from Ref. 21.

As a final note, while we exclude the hydrogen bonding model (see Chapter 3.1) as an explanation of the total stress state in our films, we do not preclude the possibility of bombarded hydrogen influencing the stress state – as the aforementioned model (to our knowledge) makes no claims of the origin of the varying hydrogen content in the films, the theories could in fact be complementary: implantation of SiH_X radicals (as suggested by Smets[29]) would account for the correlation between compressive stress and hydrogen content observed by Cammarata,[33] and our analysis/model does not depend on the specific injected species (Si, H, or, most likely, a combination of the two) actually

causing the induction of stress.

3.4. Void Collapse Effects on Stress

Through investigating the interplay between the effect of ion momentum (Eq. 11), on film porosity/density and film stress, we are able to clarify the underlying mechanisms responsible for tensile stress creation in our films.

Per Sec. II-D, the area under the ~2090 cm^{-1} infrared absorption peak is proportional to the concentration of hydrogen present in voids throughout the film, providing a numerical indication of void concentration. Figure 3.4.1b (in agreement with results observed by Hamers,[39,40] Smets,[29] and Wank[41] indicates that increasing ion momentum results in an initially rapid decrease in film porosity in the tensile region, followed by a nearly invariant low porosity in the compressive region.

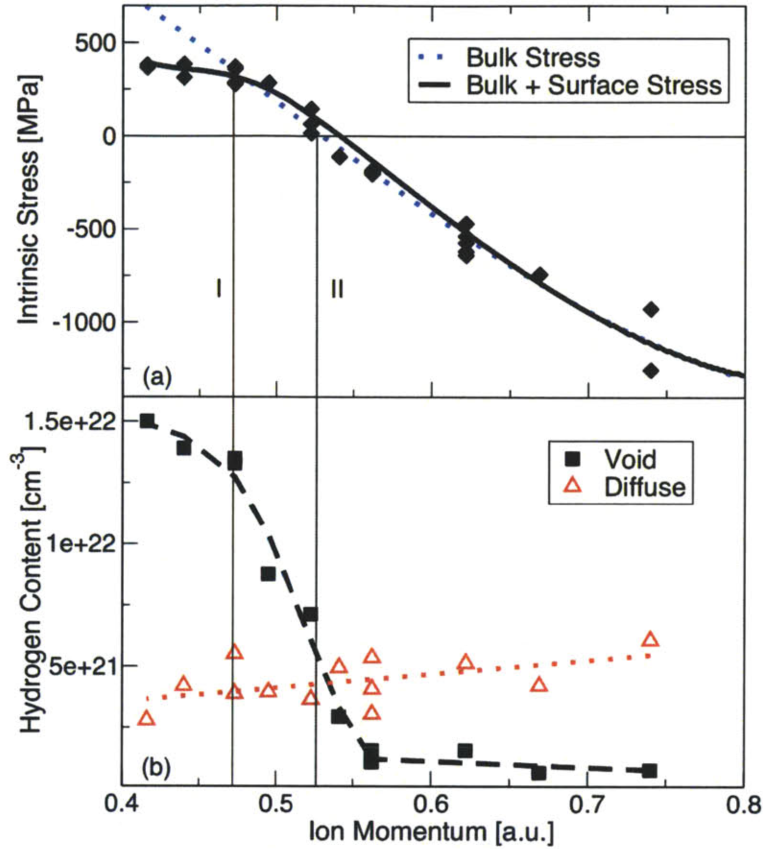

Figure 3.4.1. Film intrinsic stress as a function of ion momentum

(a): Ion momentum, $\bar{p}_{\text{ion}}$, defined in Eq. 11, shown with the fits to compressive stress (Eq. 14) and net (compressive + tensile) stress. (b): Hydrogen content and distribution in IR bonding configurations correlated to deposition ion momentum, with regressions shown as guides to the eye. Regions I and II are described in the text. Figure reprinted from Ref. 21.

We propose the modeling of tensile stress creation as proportional to the reduction of film porosity through the subtraction of the observed film hydrogen void concentration from an arbitrary baseline (representing the inherently created void concentration – see

below). Combined with the trend of compressive stress arising from bulk effects (Eq. 14) we can reproduce the net stress influence displayed as the solid line in Figure 3.4.1a, capturing the rounding of the stress-ion momentum curve (as seen in region I in Figure 3.4.1a), as well as maintaining the previously fit compressive regime (region II in Figure 3.4.1a). We dedicate the remainder of this subsection to justifying the two remaining assumptions of this model: first, that the two stress forces (compressive and tensile) apply across all deposition conditions, and second, that surface void formation is constant across our deposition conditions, with the observed reduction in hydrogen void concentration due purely to void collapse, and thus proportional to the level of tensile stress introduced.

Three aspects of our data support the conclusion that there are two independent stress forces applying across the entire range of our deposition conditions: first, the transition from tensile to compressive stress dominating in the films (shown as the beginning of region II in Figure 3.4.1) occurs well before hydrogen void concentration has reached its minimum in the films. This shows that the concentration of voids is continuing to be reduced in films well into the compressive stress regime, indicating that the tensile stress component is still present in the compressive regime, but merely being outweighed by the stronger implantation influences. Second, our model of compressive stress remains accurate far into the tensile regime, only beginning to deviate in region I, leveling off at the same location where film porosity begins to plateau as well, implying that even in the tensile stress regime, compressive stress is still playing a role in the net film stress state as well. Finally, we observe that silicon monohydride content (Figure

3.4.1b) increases continuously with ion momentum, suggesting that bulk particle implantation of hydrogenated Si (the mechanism supposed to be responsible for the silicon monohydride in the material[29]) is occurring uniformly throughout our deposition range, and providing further evidence that bulk ion bombardment is indeed occurring throughout all deposition conditions, and lending credence to the theory that void collapse occurs from bulk bombardment even at low ion momentum levels. From this information we conclude that stress creation does indeed appear to be a balance between two separate phenomena responsible for tensile and compressive forces: In region I, the hydrogen void concentration is high, indicating that the level of void collapse is low, and thus the tensile stress is relatively low as well, responsible for the decrease in stress from the pure implantation model (dashed line) observed here. In the transition to region II, void concentration decreases, indicating that tensile stress is increasing. Compressive stress is increasing as well, however, initially driving the net stress to zero as the implantation influence takes over and finally, in region II, into a state of net compressive stress.

In our model of tensile stress creation we assert that the creation of porous nanovoids from the films surface evolution is fairly constant across our deposition conditions, which we justify here though the exclusion of the plausible mechanisms for altering the surface deposition geometry: while we are exploring the influence of ion bombardment on stress and structural properties, we are modifying this parameter through control of the deposition chamber pressure, which could possibly result in unintentional effects on the depositing surface geometry via changes to the plasma and

depositing species stoichiometry, and through deviations in the deposition rate. As indicated by Doyle[42] and Gallager,[36] however, both the plasma composition and the depositing species across our process conditions should remain quite constant, which invalidates any influence that changes silane decomposition could have on the deposition surface (see Chapter 3.1). Furthermore, while we do indeed observe fairly significant changes in the film rate of deposition, McCaughey[43] and Jalali-Jafari[30] have both demonstrated through molecular dynamics simulations that decreasing film deposition rate is shown to have either no effect, or to actually increase the inherent void creation, and conclude (as we assert here) that it is ion impact effects causing the observed decline in void concentration with increasing deposition rate (which we capture in the isolated compressive stress component model). Finally, we have measured surface roughness by atomic force microscopy (AFM), which shows no correlation to deposition conditions, further assuring us that the surface evolution is not being substantially altered by changes to the process pressure. From these factors, and the quality of the fit of the net stress (solid line in Figure 3.1.1 and Figure 3.4.1a) we conclude that tensile stress can be adequately modeled as proportional to the decrease in the film hydrogen void concentration from a constant level.

3.5. Correlation between Film Density and Optical Properties

Optical properties of thin films for photovoltaic applications are of critical importance – a properly selected refractive index can limit reflection off the front surface of the cell, increasing the total light being absorbed; as well as increasing the reflections inside the back surface, thereby allowing thinner cells with a fixed absorption. Tuning of the optical bandgap is also an extremely desirable property, allowing multi-junction cells to be made controlled energy level steps, thus permitting optimization of the stack efficiency.

Film optical properties are demonstrated to correlate with changes in atomic structure of a-Si films. Figure 3.5.1 illustrates the dependences of the real and imaginary components of the refractive index and optical bandgap with density and stress. The film optical bandgap determines the cutoff in light energy that the material will absorb – for example a material with an optical bandgap of 1.6 eV will not substantially absorb light with energies below this level. The bandgap also determines the nominal open circuit voltage of a cell, so tuning of the value to an optimal position is very important for cell efficiency maximization. We observe an optical bandgap tunable from around 1.52 eV up to above 1.75 eV.

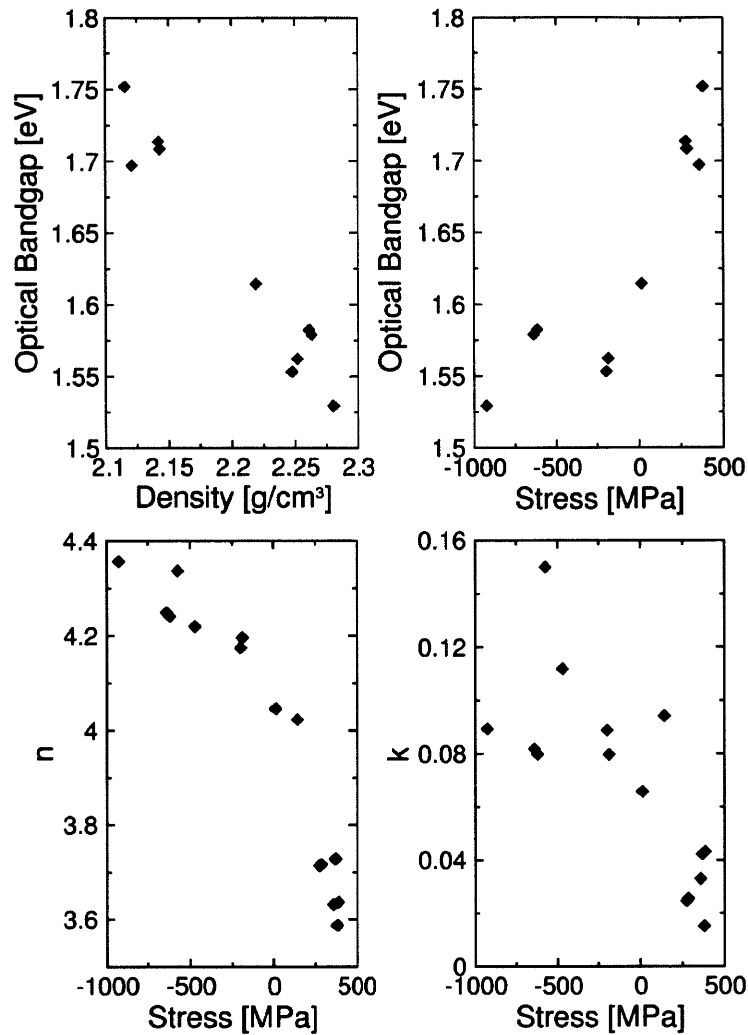

Figure 3.5.1 Optical properties as a function of stress and density

Optical properties (real [n] and imaginary [k] components of the refractive index, and optical bandgap) are plotted as a function of film structural properties (film stress and density). Plots of refractive index vs. density are omitted as the real refractive index is used to calculate our density, rendering any comparisons irrelevant.

The real component of the index of refraction, *n*, determines the velocity of light inside the material, and thereby adjusts the refraction of light as it enters the material

from an environment with a differing refractive index. This permits light to be directed, or trapped in a material, as larger differences between the environment and the material refract light more strongly. A gradated series of refractive index materials also allows decreased reflection off the surface of a material, as the lack of an abrupt change prevents strong refraction. Values of n were tunable from approximately 3.6 up to almost 4.4. The values are taken for a light wavelength of 530 nm (in air), the wavelength that represents the peak power intensity in the solar spectrum.

The complex index of refraction, k, determines the attenuation, or absorption, of light as it passes through a material. High values of k are beneficial for absorption of light at the given wavelength. The values of complex refractive index of our films were adjustable from below 0.02 up to 0.15, again taken at a light wavelength of 530 nm. Note that density is calculated via the real part of the refractive index, thus we do not display the relationship between these two variables.

A strong correlation between optical bandgap and film density is observed over the entire range of densities. On the other hand, stress and optical properties appear to have a strongest correlation in the tensile stress regime. We observe an increasing optical bandgap with increasing tensile stress (reducing density). Other authors[44,45] reported a similar trend, and speculated that it may be due to a changing of band tail states, as suggested by the model of Wagner *et al.*[46] Furthermore, density appears to correlate even more strongly with the optical bandgap. This observation suggests that film density, and not stress, has the strongest effect on film optical properties.

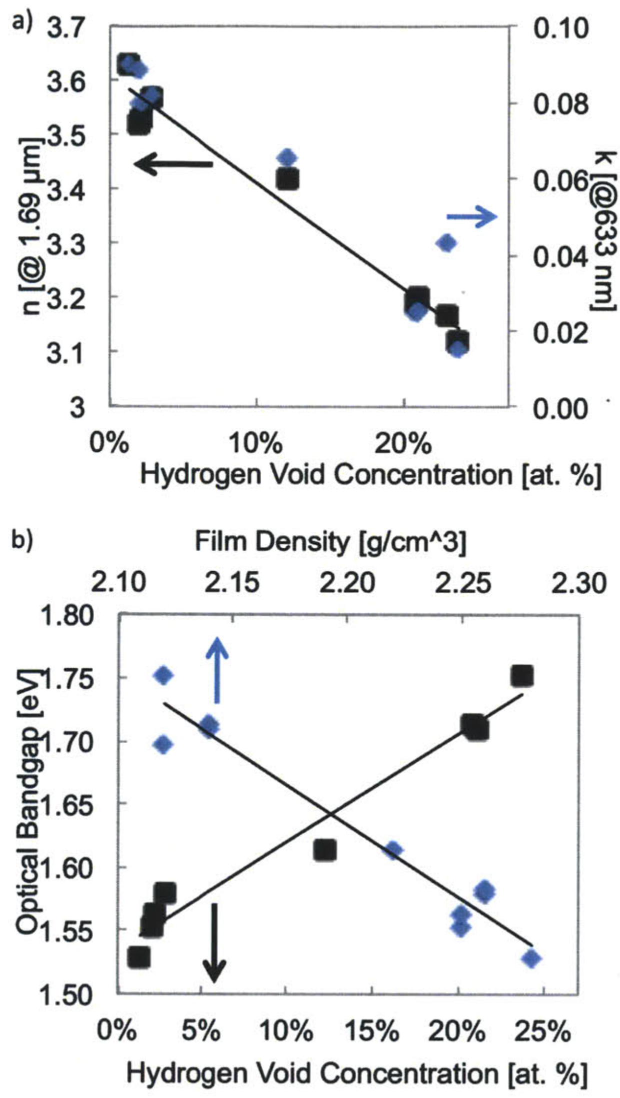

Figure 3.5.2 Relationship between hydrogen void concentration and film density

Optical properties (real [*n*] and imaginary [*k*] components of the refractive index, and optical bandgap) plotted as a function of film hydrogen void concentration, and also compared to the relationship between optical bandgap and film density

We can furthermore correlate these optical properties to the hydrogen void concentration of our films. As shown in Figure 3.5.2, linear relationships between the

refractive indices and bandgap with respect to the void concentration are observed, similar to those seen with film density. As the void concentration correlates strongly with density, the observed linear relation observed is expected.

3.6. Failure of Stressed a-Si Films

Stable films were grown with intrinsic stresses ranging from -1253 to +387 MPa. Outside this stress range, one observes film buckling (compressive failure mode, Figure 3.1.2a) and delamination (tensile failure mode, Figure 3.1.2b). Extrapolation of the stress within failed films from their operating conditions predicts buckling and delamination film failure at approximately -1200 MPa and +450 MPa, respectively.

Two trends in our data are consistent with conclusions of other studies that applied mechanical stress to a-Si films at room temperature: (1) failure under tension occurs at lower absolute stress levels than under compression,[5,6,9,44,47] and (2) the absolute magnitude of compressive stress possible without failure is on the order of 1 GPa.[6,9,44]

CHAPTER

4

CONCLUSIONS AND FUTURE WORK

4.1. Conclusions

The results of this study provide an enhanced understanding of the relationship between deposition conditions, material structure, and film properties, specifically elucidating the origins of stress within a-Si:H thin films. We begin by presenting a strong dependence of the controlled deposition process pressure on the observed film intrinsic stress, demonstrating an ability to engineer a wide range of stresses (up to 1GPa) in our a-Si:H films.

We proceed with connecting the process pressure, as well as other deposition process parameters such as RF discharge power and the RF frequency, to the ion momentum of the deposition plasma, as well as logically excluding the potential influence of any other known factors substantially influencing stress in the material.

We then develop a semi-empirical model relating ion momentum to stress creation and demonstrate further evidence of the microstructural forces contributing to

stress in amorphous silicon. We show that compressive stress varies nearly linearly with depositing ion momentum, and is controlled by ion peening of the material causing bond strain within the bulk. We then include the tensile stress forces, modeled as being controlled by hydrogen void destruction, with the void density being directly related to level of void collapse (measured through the final void concentration in the films). We provide significant evidence showing that the total intrinsic stress results from the balance between these two influences, and present the culmination of this model, featuring its ability to explain the observed stress states throughout the entire range of strongly tensile, to unstressed, to strongly compressive.

Finally, we provide observed trends of the variation in the real and imaginary refractive indices and optical bandgap dependent on measured film microstructural parameters. These optical parameters are critical for the optimization of both single- and multi-junction photovoltaic cells, and the determined ability to tune these parameters should permit finer optimization of created devices, as well as simplifying the introduction of amorphous silicon materials into the development of other photonics-relevant fields.

4.2. Future Work

From these results, in combination with recent electrical transport[48,49] and optical measurements[41] reported elsewhere, a more complete picture of a-Si:H film process-

structure-property relations begins to emerge. With the ability to predict film microstructure structure using empirical models, controllable a-Si:H properties should be achievable on a wide range of deposition systems.

We are currently working to correlate the controlled deposition parameters of a-Si:H film creation to the mobility of the films, a parameter critical to moving the efficiency of amorphous silicon-based PV devices beyond their currently limited level. A major challenge in this work will be deconvolving the influence of the multitude of varied factors (microstructure, optical properties, stress, etc.) discussed herein on the potentially observed changes of mobility in the deposited films.

APPENDIX

Experimental details of a representative subset of samples investigated in this study. Variables not listed are equal to the baseline process (described in Chapter 2.1). Samples exhibiting some failure mechanism that invalidates the assumptions of Stoney's formula (Chapter 2.2) are not included.

ID	Deposition Conditions				Film Stress			Film Properties			
	Pressure [mTorr]	**Film Thickness** [nm]	**Calculated Normalized Ion Momentum** [a.u.]	**Calculated Deposition Rate** [Å/s]	**Total a-Si Stress** [MPa]	**Calculated Thermal Stress** [MPa]	**Calculated Intrinsic Stress** [MPa]	**Calculated a-Si Film Density** [g/cm^3]	**Real Refractive Index** [@633 nm]	**Imaginary Refractive Index** [@633 nm]	**Optical Bandgap** [eV]
1	100	784	0.181	1.8	-910.6	14.3	-924.9	2.28	4.36	0.09	1.53
2	200	186	0.126	2.2	-625.2	14.0	-639.2	2.26	4.25	0.08	1.58
3	200	172	0.128	2.1	-605.1	14.0	-619.1	2.26	4.24	0.08	1.58
4	300	1861	0.061	4.1	-184.1	12.7	-196.8	2.25	4.17	0.09	1.55
5	300	355	0.065	3.8	-172.6	12.9	-185.5	2.25	4.20	0.08	1.56
6	400	1434	0.047	5.1	26.4	12.0	14.4	2.22	4.05	0.07	1.61
7	600	178	0.022	9.9	287.1	8.7	278.4	2.14	3.71	0.02	1.71
8	600	177	0.022	9.8	295.7	8.7	287.1	2.14	3.72	0.03	1.71
9	600	261	0.021	10.7	367.8	8.1	359.7	2.12	3.63	0.03	1.70
10	1000	206	0.017	11.5	388.5	7.5	381.0	2.12	3.59	0.02	1.75

Table 0.1 Film properties of representative samples

ACKNOWLEDGEMENTS

I would like to acknowledge and thank, first, my advisors Tonio Buonassisi, and Jeff Grossman, second, the post-docs who helped me with this work, Christie Simmons and Lucas Wagner, and finally our collaborators at the King Fahd University of Petroleum and Minerals (KFUPM), Nouar Tabet, Syed Said, and Amir Abdallah. I would also like to acknowledge and thank Physical Review B of the American Physical Society for not only publishing this work, but allowing it to be used in this thesis under their standard copyright agreement.

I would like to thank the King Fahd University of Petroleum and Minerals in Dhahran, Saudi Arabia, for funding the research reported in this paper through the Center for Clean Water and Clean Energy at MIT and KFUPM under project number R1-CE-08. This work was performed in part at the Center for Nanoscale Systems (CNS), a member of the National Nanotechnology Infrastructure Network (NNIN), which is supported by the National Science Foundation under NSF award no. ECS-0335765.

REFERENCES

[1] D.M. Powell, M.T. Winkler, H.J. Choi, C.B. Simmons, D.B. Needleman, and T. Buonassisi, Energy Environ. Sci. **5**, 5874–5883 (2012).

[2] Greentech Media Research, PV News **31**, 1–28 (2012).

[3] S. Hegedus, Progress in Photovoltaics: Research and Applications **14**, 393–411 (2006).

[4] H. Gleskova, S. Wagner, W. Soboyejo, and Z. Suo, Journal of Applied Physics **92**, 6224 (2002).

[5] H. Gleskova, I. Cheng, S. Wagner, J. Sturm, and Z. Suo, Solar Energy **80**, 687–693 (2006).

[6] H. Gleskova, P. Hsu, Z. Xi, J. Sturm, Z. Suo, and S. Wagner, Journal of Non-Crystalline Solids **338-340**, 732–735 (2004).

[7] M.C. Wang, T.C. Chang, P.-T. Liu, S.W. Tsao, Y.P. Lin, and J.R. Chen, Electrochemical and Solid-State Letters **10**, J113 (2007).

[8] R.B. Wehrspohn, S.C. Deane, I.D. French, I. Gale, J. Hewett, M.J. Powell, and J. Robertson, Journal of Applied Physics **87**, 144–154 (2000).

[9] J. Gaspar, O. Paul, V. Chu, and J.P. Conde, Journal of Micromechanics and Microengineering **20**, 035022 (2010).

[10] J. Dutta, U. Kroll, P. Chabloz, A. Shah, A.A. Howling, J.L. Dorier, and C. h. Hollenstein, Journal of Applied Physics **72**, 3220–3222 (1992).

[11] E. Johlin, S. Castro-Galnares, A. Abdallah, N. Tabet, M.I. Bertoni, T. Asafa, J.C. Grossman, S. Sayed, and T. Buonassisi, in *2011 37th IEEE Photovoltaic Specialists Conference* (2011), pp. 000176–000178.

[12] L.B. Freund and S. Suresh, *Think Film Materials: Stress , Defect Formation and Surface Evolution* (2003).

[13] N. Layadi, P.R. Cabarrocas, and B. Drevillon, Physical Review B **52**, 5136 (1995).

[14] Y. Hishikawa, N. Nakamura, S. Tsuda, S. Nakano, Y. Kishi, and Y. Kuwano, Japanese Journal of Applied Physics **30**, 1008–1014 (1991).

[15] Z. Remeš, M. Vaneček, P. Torres, U. Kroll, A.H. Mahan, and R.S. Crandall, Journal of Non-Crystalline Solids **227**, 876–879 (1998).

[16] A.A. Langford, M.L. Fleet, B.P. Nelson, W.A. Lanford, and N. Maley, Physical Review B **45**, 13367 (1992).

[17] A.H. Mahan, L.M. Gedvilas, and J.D. Webb, Journal of Applied Physics **87**, 1650–1658 (2000).

[18] H. Shanks, C. Fang, L. Ley, M. Cardona, F. Demond, and S. Kalbitzer, Physica Status Solidi (b) **100**, 43–56 (1980).

[19] A.H.M. Smets, W.M.M. Kessels, and M.C.M. van de Sanden, Applied Physics Letters **82**, 1547 (2003).

[20] P.J. Zanzucchi, C.R. Wronski, and D.E. Carlson, Journal of Applied Physics **48**, 5227 (1977).

[21] E. Johlin, N. Tabet, S. Castro-Galnares, A. Abdallah, M.I. Bertoni, T. Asafa, J.C. Grossman, S. Said, and T. Buonassisi, Physical Review B **85**, 075202 (2012).

[22] M. Ohring, *Materials Science of Thin Films, Second Edition* (Academic Press, Boston, 2001), p. 794.

[23] Y. Fu, J. Luo, S. Milne, A. Flewitt, and W. Milne, Materials Science and Engineering: B **124-125**, 132–137 (2005).

[24] J.H. Lee, D.S. Kim, Y.H. Lee, and B. Farouk, Journal of The Electrochemical Society **143**, 1451–1458 (1996).

[25] A.D. Glew, R. Saha, J.S. Kim, and M.A. Cappelli, Surface and Coatings Technology **114**, 224–229 (1999).

[26] V. Kulikovsky, V. Vorlíček, P. Boháč, M. Stranyánek, R. Čtvrtlík, and a. Kurdyumov, Thin Solid Films **516**, 5368–5375 (2008).

[27] H. Windischmann, Journal of Applied Physics **62**, 1800–1807 (1987).

[28] H. Windischmann, Journal of Vacuum Science & Technology A **9**, 2431–2436 (1991).

[29] A.H.M. Smets, W.M.M. Kessels, and M.C.M. van de Sanden, Journal of Applied Physics **102**, 073523 (2007).

[30] B. Jalali-Jafari, H. Savaloni, and M. Gholipour-Shahraki, Physica Status Solidi (B) **244**, 3620–3638 (2007).

[31] K.-H. Müller, Journal of Applied Physics **62**, 1796 (1987).

[32] C.A. Davis, Thin Solid Films **226**, 30–34 (1993).

[33] R.C. Cammarata, Progress in Surface Science **46**, 1–38 (1994).

[34] Y. Hishikawa, Journal of Applied Physics **62**, 3150 (1987).

[35] A. Matsuda, Journal of Non-Crystalline Solids **59**, 767–774 (1983).

[36] A. Gallagher, Journal of Applied Physics **63**, 2406–2413 (1988).

[37] Y. Catherine and P. Couderc, Thin Solid Films **144**, 265–280 (1986).

[38] C. Miranda, K. Tretiakov, and S. Scandolo, Journal of Non-Crystalline Solids **352**, 4283–4286 (2006).

[39] E.A.G. Hamers, Acta Physica Slovaca **50**, 533–544 (2000).

[40] E.A.G. Hamers, W. van Sark, J. Bezemer, H. Meiling, and W.F. van der Weg, Journal of Non-Crystalline Solids **226**, 205–216 (1998).

[41] M.A. Wank, R.A.C.M.M. van Swaaij, P. Kudlacek, M.C.M. van de Sanden, and M. Zeman, Journal of Applied Physics **108**, 103304 (2010).

[42] J.R. Doyle, D.A. Doughty, and A. Gallagher, Journal of Applied Physics **68**, 4375 (1990).

[43] M.J. McCaughey and M.J. Kushner, Journal of Applied Physics **65**, 186–195 (1989).

[44] T.N. Ng, W.S. Wong, R. a. Lujan, and R. a. Street, Advanced Materials **21**, 1855–1859 (2009).

[45] X. Jiang, K. Reichelt, and B. Stritzker, Journal of Applied Physics **66**, 5805 (1989).

[46] L.K. Wagner and J.C. Grossman, Physical Review Letters **101**, 265501 (2008).

[47] H. Gleskova, S. Wagner, and Z. Suo, Applied Physics Letters **75**, 3011 (1999).

[48] M.A. Wank, R. van Swaaij, R. van de Sanden, and M. Zeman, Progress in Photovoltaics: Research and Applications **20**, 333–342 (2012).

[49] G. Ganguly, I. Sakata, and A. Matsuda, Journal of Non-Crystalline Solids **198**, 300–303 (1996).